

Corrosion of Ductile Cast Iron Pipeline in a Water Supply Network Based on the Flow Field Changing

*Chuntong Liu, Yimei Tian, Rufang Zhang, Xingfei Liu, Hao guo, Yarong Song, Sen Peng**

Department of Environmental Engineering, School of Environmental Science and Engineering, Tianjin University, Tianjin 300350, China

*E-mail: pengsen_tju@126.com

Received: 6 May 2018 / Accepted: 11 July 2018 / Published: 5 August 2018

In this work, a computational fluid dynamics (CFD) simulation and electrochemical measurements are performed to study corrosion at different positions of the elbow and its adjacent areas in water supply pipelines using two designed pipe fittings on a dynamic corrosion platform. The corrosion passive film on the ductile cast iron surface is the primary control factor in the corrosion process. Furthermore, although corrosion activity occurs more frequently at the innermost portion of the elbow and the outer portion of the downstream straight sections, corrosion at the top (or bottom) and outer side of the elbow occurs less often.

Keywords: A. Iron, B. EIS, C. Anodic dissolution

1. INTRODUCTION

With the increasing shortage of water resources, water security has become an important factor that limits urban construction and impacts residents' lives[1]. However, pipe corrosion, pipe bursts and other pipe network deterioration situations have affected the normal operations of urban water supply systems, and thus it is one of the first problems that should be solved to achieve urban water supply security[2]. It has been acknowledged that water supply pipeline corrosion can cause pipeline failure and water quality deterioration, thus resulting in the secondary pollution of tap water and greater energy consumption and substantial economic loss[3-5]. The corrosion of the water supply pipeline is a complex process with a number of factors being affected simultaneously[6, 7]. For example, the fluid hydrodynamics effect is significant as it accelerates the mass transfer process and destroys the protective corrosion product layer, thus promoting corrosion[8-10].

Early in the 1990s, Nešić and Postlethwaite introduced the computational fluid dynamics (CFD) method to simulate flow field distribution and discuss the impact of hydrodynamics on near-wall fluid

corrosion[11, 12]. Since then, the CFD method has been widely used in high-speed and high-temperature erosion of cyclical pipelines in nuclear power plants and numerical simulations of fluid accelerated corrosion (FAC) in oil-gas multiphase flow engineering[8, 9, 12-16]. It has laid a theoretical foundation for applying the numerical simulation of fluid dynamics calculations of water supply pipeline corrosion.

In water supply and transportation networks, the elbow is a typical part of pipe configurations; the fluid hydrodynamics in the elbow are fierce and changeable, especially in a 90° elbow[17, 18]. Therefore, the corrosion behaviour at the elbow and its adjacent areas cannot be ignored. Furthermore, the extent of corrosion is significantly distinct at different positions of the elbow pipe fitting. Finding the most likely location near the elbow for corrosion can provide a basis for manufacturing pipe fittings and reducing the risk of pipeline leakage. Currently, the majority of studies on corrosion behaviour at the elbow focus on carbon dioxide-based corrosion in oil-gas pipelines, especially with respect to steel pipes[8-10, 19]. Corrosion at the elbow and its adjacent areas of ductile cast iron pipelines in water supply networks, however, has not been as well explored.

In this work, a dynamic corrosion platform is used to simulate the actual corrosion of water supply pipelines, and two types of 90° elbow pipe fittings are designed to investigate the difference in corrosion behaviour according to different positions of the elbow using a CFD simulation and electrochemical measurements.

2. EXPERIMENTAL

2.1 Materials and solutions

The test specimens in this work were made of a QT500-10 ductile cast iron rod with a chemical composition (wt.%) of C 3.3%, Si 3.7%, Mn 0.3%, P 0.05%, S 0.02%, Mg 0.04%, Cu 0.1% and Fe making up the balance. The ductile cast iron rod was cut and machined into thin rod electrodes with an exposure area of 0.5 cm². The ductile cast iron thin rod electrodes were coated with polytetrafluoroethylene (PTFE) to mount in the simulation device. The specific form is displayed in Fig. 1. All the electrodes were electrically connected individually by copper pillars to the measurement equipment. The electrodes were ground successively using metallographic sandpaper of 1000, 1200, 1500 and 2000 grit, rinsed with deionized water and degreased in anhydrous alcohol and acetone.



Figure 1. Specific form of the single electrode.

The corrosive media was tap water from the laboratory, whose characteristics are shown in Table 1. No significant changes occurred in the tap water quality during the entire experiment. All tests were

performed at room temperature (23 °C) and atmospheric pressure.

Table 1. Characteristics of the tap water.

Parameters	Value	Parameters	Value
pH	7.13 ± 0.30	TDS (mg/L)	190 ± 4.2
DO (mg/L)	6.27 ± 0.38	Conductivity ($\mu\text{s}/\text{cm}$)	550 ± 7.6
Total hardness (mgCaCO ₃ /L)	237.16 ± 9.5	Total alkalinity (mgCaCO ₃ /L)	112.11 ± 6.5
Chloride (mg/L)	48.96 ± 1.6	Sulfate (mg/L)	105.87 ± 7.6

2.2 Dynamic corrosion platform

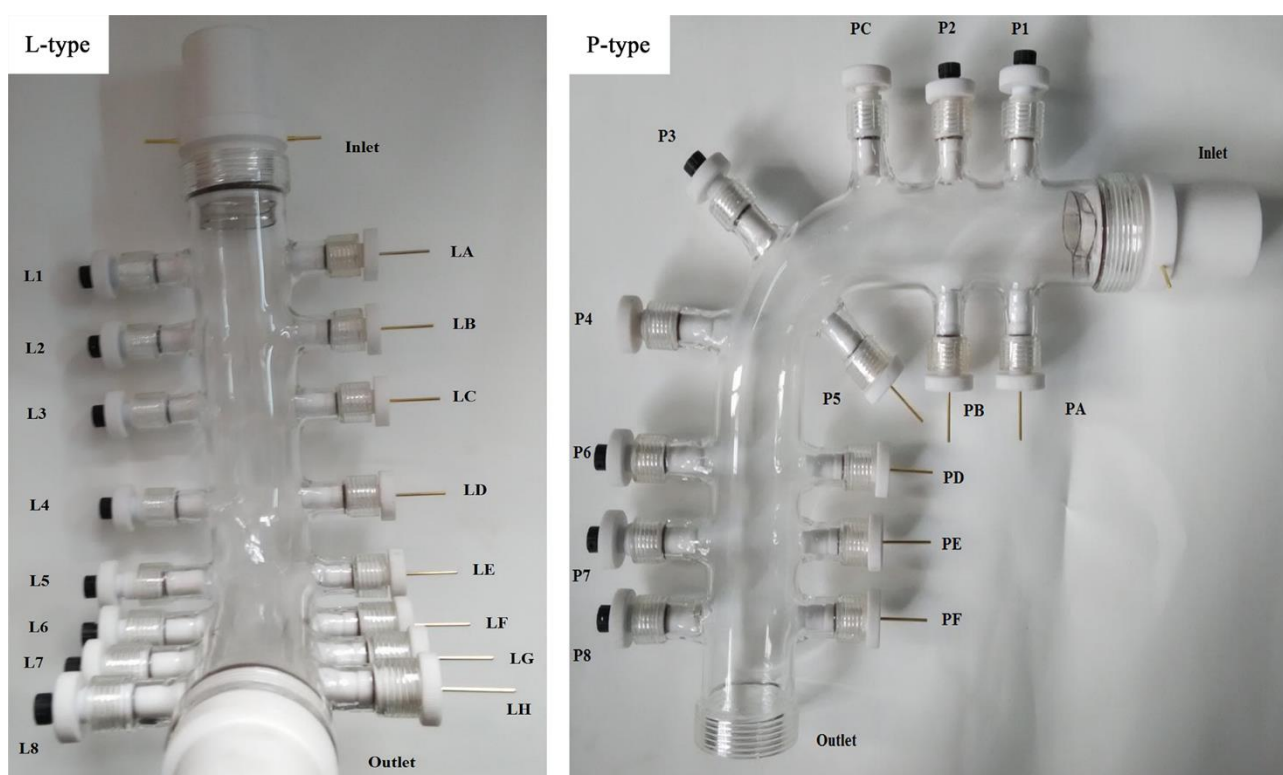


Figure 2. L-type (left) and P-type (right) elbow pipe fittings.

The typical pipe fittings in this work are two designed integrated 90° glass elbows. According to the installation site of the ductile cast iron electrode, two types of elbows are custom-made, namely, the L-type and P-type as presented in Fig. 2. The only difference between these two pipe fittings is the site of the branch, while other structures and sizes are the same. The reference electrode and the working electrode installation branch extend up and down symmetrically in the L-type pipe fitting, whereas in the P-type pipe fitting, the reference electrode and the working electrode installation branch are located on the cross-sectional centre level, revealing the inner and outer symmetrical distribution. The specific installation site of every electrode was determined by the CFD simulation results below. All the electrodes' surfaces are coplanar with the tube surface. Both ends of the tube are screw joints made of

PTFE, both with diameters of 50 mm. The upstream straight section is 150 mm long, and the downstream straight section is 200 mm long. The branch nominal outer diameter is 24 mm, and the inner diameter is 20 mm.

A dynamic corrosion platform is used to conduct the corrosion monitoring test as displayed in Fig. 3. The platform contains a water update system, a pipe circulation system and an electrochemical test system. The arrows in the figure indicate the direction of water flow.

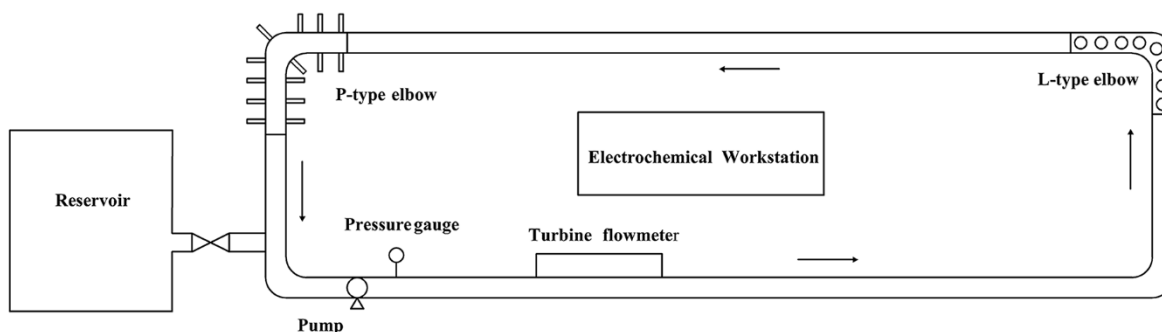


Figure 3. Dynamic corrosion platform.

2.3 CFD simulation

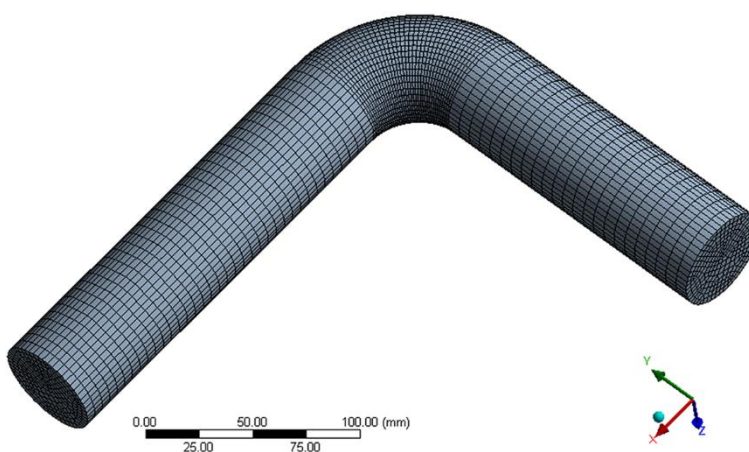


Figure 4. Meshing of model used in CFD simulation.

The CFD simulation and analysis were performed using Fluent-ANSYS Workbench 15.0 software (ANSYS, USA). The realizable $k-\epsilon$ turbulent model was used. The mesh model used in this work is presented in Fig. 4, and the number of the grid is 20000. The wall was assumed to be the no-slip boundary condition, and time was set as the steady state. At the pipe inlet, the velocity inlet boundary condition was used to define the average actual velocity of the fluid. At the outlet of the pipe, the free-outflow boundary condition was used. The fluid flow velocities of 0.5, 1.0 and 1.5 m/s were considered with corresponding inlet turbulence intensities of 4%, 5% and 6%, respectively. The hydraulic diameter was 12.5 mm.

The finite volume method and SIMPLE algorithm were used to solve the pressure-velocity coupling. The simulation was complete when the variables in each direction between the two consecutive iteration residuals were below 0.001 after the finite iteration.

2.4 Electrochemical measurements

Electrochemical measurements were conducted with a three-electrode cell using a CS2350 electrochemical workstation (Wuhan Corrtest Instruments Corp., Ltd., China), including the open circuit potential (OCP), the potentiodynamic scanning and the electrochemical impedance spectroscopy (EIS). A ductile, cast iron thin rod electrode was used as the working electrode, a saturated calomel electrode (SCE) was used as the reference electrode, and a platinum cylinder was used as the counter electrode.

The OCP was determined once every two hours. The potentiodynamic scanning was conducted at a potential sweep rate of 0.1 mV/s within the range of -50 to 50 mV versus the OCP to obtain the polarization curves. Then, the corrosion current density (i_{corr}) was determined by fitting analysis using Cview 2.0, and the corrosion rates were calculated with Equation (1)[20].

$$V = \frac{365 \cdot 24 \cdot 3600 \cdot 10 \cdot i_{\text{corr}} \cdot M}{nF\rho} \quad (1)$$

Here, V is the corrosion rate in $\text{mm} \cdot \text{a}^{-1}$, i_{corr} is the corrosion current density in $\text{A} \cdot \text{cm}^{-2}$, M is the molar mass of Fe in $\text{g} \cdot \text{mol}^{-1}$, n is the number of electrons transferred in the electrode reaction, F is Faraday's constant ($96,485 \text{ C} \cdot \text{mol}^{-1}$), and ρ is the density of ductile cast iron in $\text{g} \cdot \text{cm}^{-3}$.

In this experiment, the electrode corrosion reaction was carried out at a neutral pH. Therefore, the reaction is oxygen corrosion, and the anodic reaction is shown in Equation (2).



Therefore, the value of n is 2 in this study.

EIS measurements were carried out under OCP using a 10 mV amplitude sinusoidal signal over the frequency range of 100 kHz to 0.01 Hz.

3. RESULTS AND DISCUSSION

3.1 CFD simulation

Fig. 5 displays the contours of the fluid flow velocity field, the pressure and the streamlines at the cross-section of the pipe fitting under various inlet fluid flow velocities using CFD simulation. Fig. 5 (a, b and c) indicates that all of the maximum flow velocity occurred on the innermost side of the inner wall of the 90° elbow under three different conditions, although the area of high-velocity range is small, and that the flow velocity corresponding to the outer side of the elbow is less than that corresponding to the innermost portion of the inner wall. Moreover, the flow velocity distributions among the upstream straight sections are uniform and close to the inlet flow rate. However, the velocity distributions of the downstream straight sections are uneven where the flow separation formed due to the curvature of the elbow and the centrifugal force[15, 21]. From the inner wall of the 90° elbow, the velocity is divided

into two trends, such that the outward flow rate is higher. Furthermore, as the flow velocity increases near the inner wall, the boundary layer thins[15].

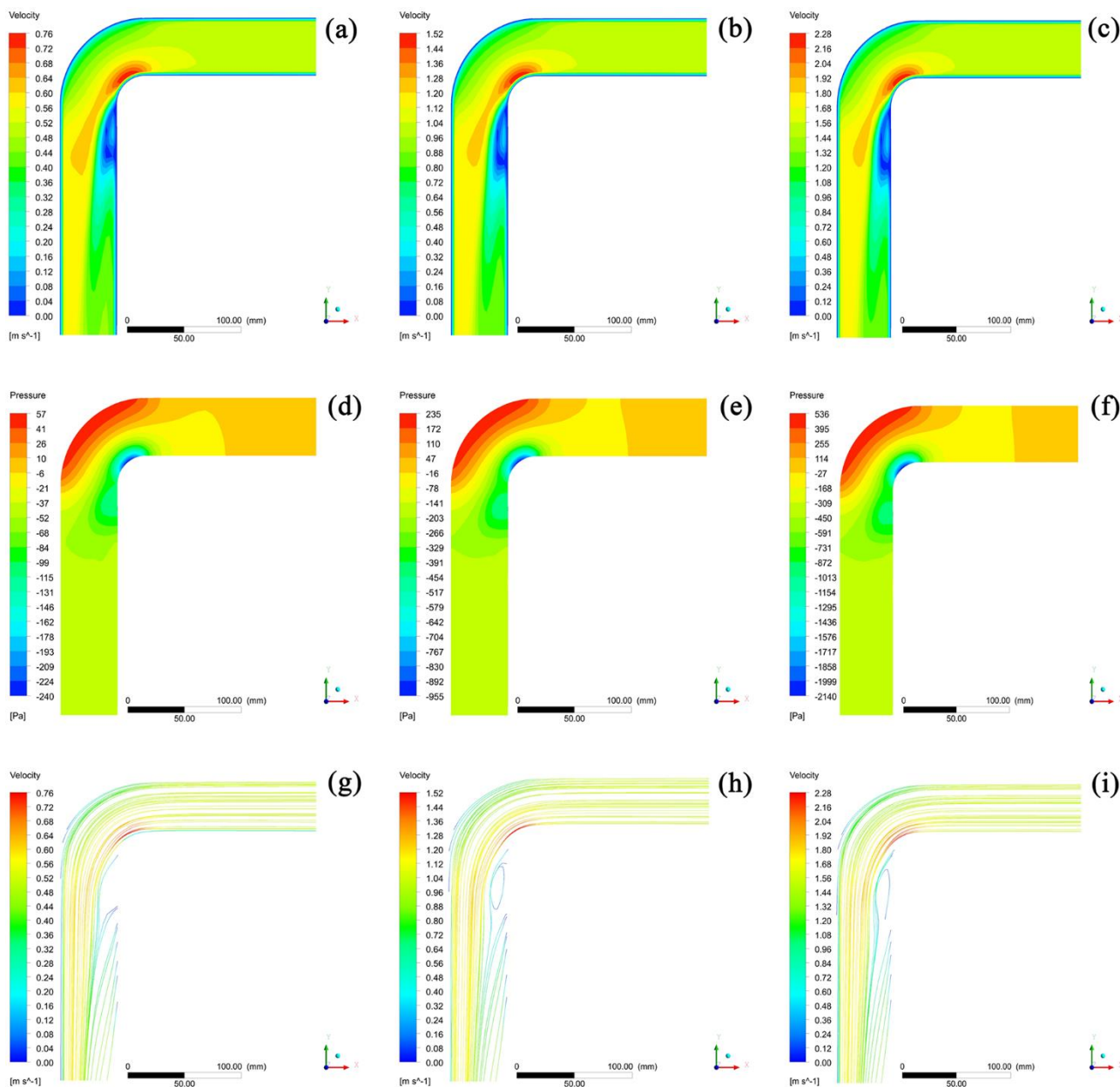


Figure 5. CFD simulation of the fluid flow velocity field distribution at the cross-section of pipe fitting at inlet fluid flow velocities of 0.5 m/s (a), 1.0 m/s (b), and 1.5 m/s (c); pressure distribution at inlet fluid flow velocities of 0.5 m/s (d), 1.0 m/s (e), and 1.5 m/s (f); and streamline contour at inlet fluid flow velocities of 0.5 m/s (g), 1.0 m/s (h), and 1.5 m/s (i).

It is noted that the pressure distribution is identical under varied conditions, as presented in Fig. 5(d, e and f) and that the distribution is opposite that of the distribution of velocity, as the maximum pressure occurs on the outer side of the 90° elbow. Similarly, due to the influence of the elbow curvature and the centrifugal force, the pressure at the outer wall increases when the flow moves along the elbow. Simultaneously, negative pressure appears at the inner side of the 90° elbow within a narrow range.

Furthermore, the maximum positive pressure and the minimum pressure vary significantly as the inlet velocity increases. Accordingly, the centrifugal force is proportional to the square of the fluid velocity, which also explains the phenomenon that radial pressure is distributed differently at the elbow. Moreover, the pressure in the upstream section is higher than that of the downstream section.

The streamline simulation results under three inlet fluid flow velocities are presented in Fig. 5 (g, h, and i). The figure indicates that adjacent to the 90° elbow and with the increase of inlet velocity, the vortex formed is more obvious and the shape and distribution of the streamlines have become increasingly more complex. Nonetheless, the streamline in the two straight sections and most of the regions maintain consistency with the shape of the pipe. The pressure difference between the inner and outer walls induces a secondary flow from the outer wall to the inner wall[18] and, due to the effect of the secondary flow, the recirculation flow appears near the inner wall[21].

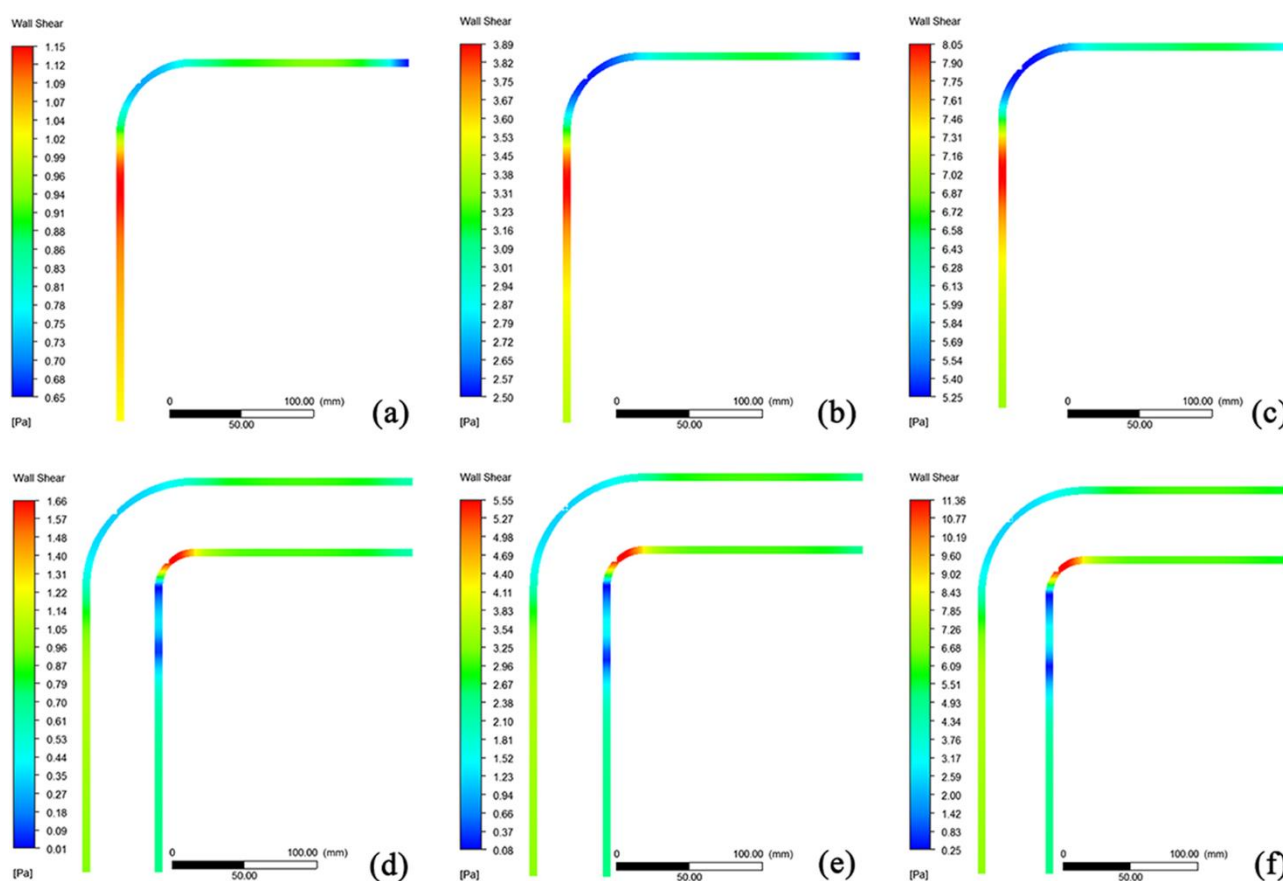


Figure 6. CFD simulation of wall shear stress distribution at the cross-section in the pipe fitting at inlet fluid flow velocities of 0.5 m/s (a), 1.0 m/s (b), and 1.5 m/s (c); and the top (bottom) of the elbow at inlet fluid flow velocities of 0.5 m/s (d), 1.0 m/s (e), and 1.5 m/s (f).

In addition to the fluid flow condition, wall shear stress plays a significant role in pipeline corrosion. When corrosion occurs, high wall shear stress can accelerate local corrosion[22]. Fig. 6 indicates the wall shear stress distribution of the pipe fitting at various inlet fluid flow velocities. As Fig. 6 (a, b, and c) indicates, shear scour at the top (or bottom) of the elbows and the straight sections mainly occurs in the downstream straight section, especially adjacent to the centre of the elbow, where the shear

scour is relatively substantial. The fluid flow distribution at the top and bottom of the pipe can be regarded as virtually identical considering the little influence of gravity. The wall shear stress distribution in the pipe fittings at the centre level are presented in Fig. 6 (d, e, and f). It is evident that shear stress at the innermost side of the elbow is relatively substantial and that the inner and outer upstream straight sections and outer downstream straight section have the same level of shear stress. The wall shear stress of the outer side of the elbow and the inner side of the downstream straight section, however, is relatively small. Nonetheless, whether it is the average or the maximum shear stress, it significantly increases as the inlet velocity increases. Furthermore, when comparing the wall shear stress on the cross-section of the pipe fitting to the top (or bottom) of the pipe fitting at the same inlet fluid flow velocity, the former is greater than the latter, regardless of the average or maximum value.

3.2 Electrode site selection

It is reasonable to monitor the valuable point and its adjacent area or the region where fluid flow direction exhibits dramatic changes and to then use these representative points to predict the overall corrosion rules. Based on the analysis of the distribution of the flow velocity field (streamline), the pressure field and the wall shear stress in pipe fittings under different inlet velocities, the specific site selection is presented in Fig. 2. In the L-type pipe fitting, there are eight electrode measuring sites. Considering that the direction of the reference electrode cannot be inverted, these working electrodes are distributed on the top of the pipe fitting corresponding to the position of the saturated calomel electrodes on the bottom of the pipe fitting. In the P-type pipe fitting, considering the distinction of the distribution characteristics of the flow field at the inner side and the outer side the elbow, seven sites are located at the outer side of the pipe fitting, and one site is identified at the inner side of the pipe fitting. Given this condition, working electrodes P3 and P5 use a common reference electrode PC, and working electrodes P4 and P6 use a common reference electrode PD. This is because the test of the P5 site is more valuable than the PC site when all research points are measured simultaneously. Thus, the reliability of the results is ensured.

3.3 Determination of experimental period

The long-term monitoring of the corrosion process can be achieved via an electrochemical measurements system. However, with the progress of the electrochemical reaction, the ductile cast iron electrode matrix dissolves and generates Fe^{2+} , and the dissolved oxygen in the water continually reacts with the Fe^{2+} , thus generating $\text{Fe}(\text{OH})_n$ and other water-soluble corrosion products that covered the electrodes, according to the Pourbaix diagram analysis, because the tap water is weakly alkaline. However, because the metal electrode surface area is only 0.5 cm^2 , when corrosion reaches a certain stage, there will be a case similar to the process where outer biofilms decline and inner biofilms would grow during waste water treatment processes[23]. This phenomenon occurs periodically on the surface of the electrode, indicating that corrosion enters into a stable development stage, i.e., OCP changes steadily, and, subsequently, the random fluctuations effects due to the early unstable corrosion can be

excluded[24].

Therefore, before the typical pipe fitting dynamic corrosion test, it is necessary to test for the stability time under the parameters of the experimental electrode system. Thus, electrodes P5 and L6 are chosen to represent the elbow and its adjacent area, respectively, due to the large number of electrodes. The test results of the OCP changes at an inlet velocity of 1.5 m/s over 168 h are presented in Fig. 7. Fig. 7 indicates there exist three stages relevant to both P5 and L6, namely, a fluctuating initial corrosion stage (0 to 24 h), a gradual decline to a stabilization transition stage (24 to 48 h), and a stable balanced stage with small changes (48 h to 168 h). It is concluded that the changes in the OCP plateau after approximately 48 h.

The OCP electrode characterizes the difficulty of the electrode corrosion reaction under natural conditions, a reaction that is closely related to the electrode surface coverage and the response degree[25, 26]. During this extended period of 168 h, electrode OCP stability observation measurements before the dynamic corrosion test are recorded, and it is taken into account that the hydrodynamic property changes of P5 and L6 at an inlet velocity of 1.5 m/s are dramatic and significantly representative compared to other study points. Thus, it can be determined that after 48 h, the surface corrosion reactions of the electrodes have stabilized under this dynamic electrochemical corrosion experiment platform. Accordingly, it is reasonable to determine the experimental period as 144 h.

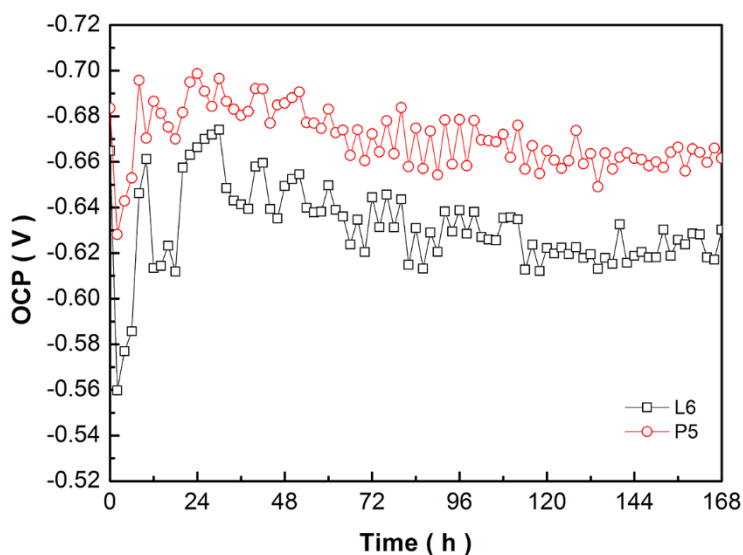


Figure 7. OCP changes on electrode L6 and P5 at an inlet velocity of 1.5 m m/s over 168 h.

3.4 OCP measurements

To exclude the impact on the experiment caused by the inherent differences of the electrodes and to obtain the basic value of the electrochemical parameters under corrosive environments in this pipe fitting, OCP monitoring is conducted in a stationary state. As it can be considered that there is no difference in the flow field distribution between the L-type and P-type pipe fittings given a stationary state, the P-type pipe fitting is chosen as the electrode carrier in this study. The OCP measurement results

are presented in Fig. 8. Fig. 8 indicates that the OCP of almost every study electrode fluctuates around its stable value of approximately 0.002 V as they become stable after 48 h. The range of the stable OCP values among these eight electrodes is less than 0.01 V, an error that is acceptable considering unavoidable disturbances and the fact that the electrodes are manually ground.

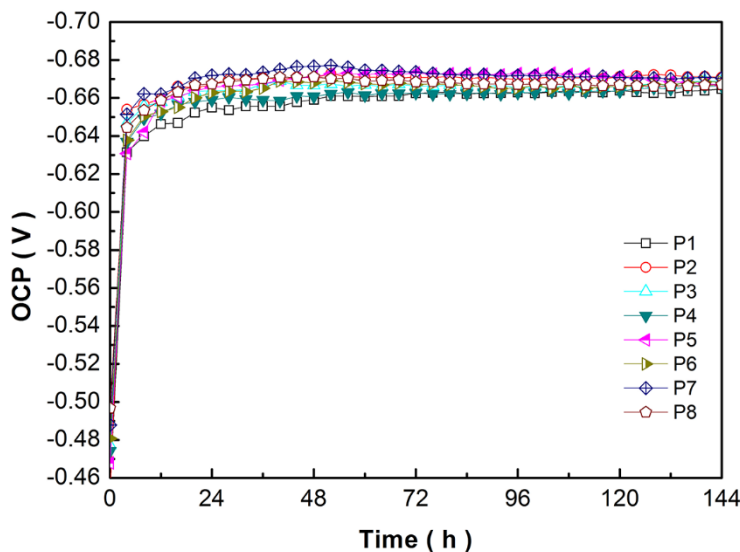


Figure 8. OCP measurements of P-type pipe fitting in a stationary state.

Fig. 9 presents the OCP measurements of the L-type and P-type pipe fittings at the three inlet velocities. It also indicates that the OCP measurements at all research sites stabilized after 120 h, though a steady growth trend was observed later. Furthermore, the OCP increases slightly throughout the course of the reaction time. This observation is attributed to the accumulation of corrosion products and intermediates on the surface of the electrodes, as such coverings play a protective role that slows down, to a certain extent, further corrosion[27]. Furthermore, site L5, which is located at the top of the junction of the downstream straight section and the elbow, experiences the highest OCP of all electrodes on the L-type pipe fitting, as indicated in Fig. 9 (a, b, c). Though the distinction among the remaining seven sites is not as obvious, the OCPs of L1, L2, L3 and L4 are somewhat higher than the OCPs of L6, L7 and L8, suggesting that the corrosion tendency in the upstream straight section is weaker than that in the downstream straight section. Similarly, regardless of the inlet velocity, the highest OCP is observed on electrode P3, which is located at the outer side of the elbow, whereas electrode P5, which is located at the inner side of the elbow, exhibits the lowest OCP among the electrodes on the P-type pipe fitting. Furthermore, site P4 exhibits a relatively high OCP, while the other five sites fluctuate within a narrow range. Coincidentally, sites L3, L4, L5, P3 and P4 are located at the top and outer side of the elbow, where the flow velocity and wall shear stress are the lowest and the pressure is the highest. Thus, the higher OCPs in these sites may be because the low flow velocity and wall shear stress are barely capable of destroying the stable surface structure. Simultaneously, the high pressure, which is perpendicular to the outward wall, may exhibit a fixed action on the corrosion product layer or the deposit layer on the surface of the electrodes, thus promoting the formation of such layers and decreasing the tendency of corrosion. For changes regarding OCP, the L5 and P3 study sites reflect more stable corrosion.

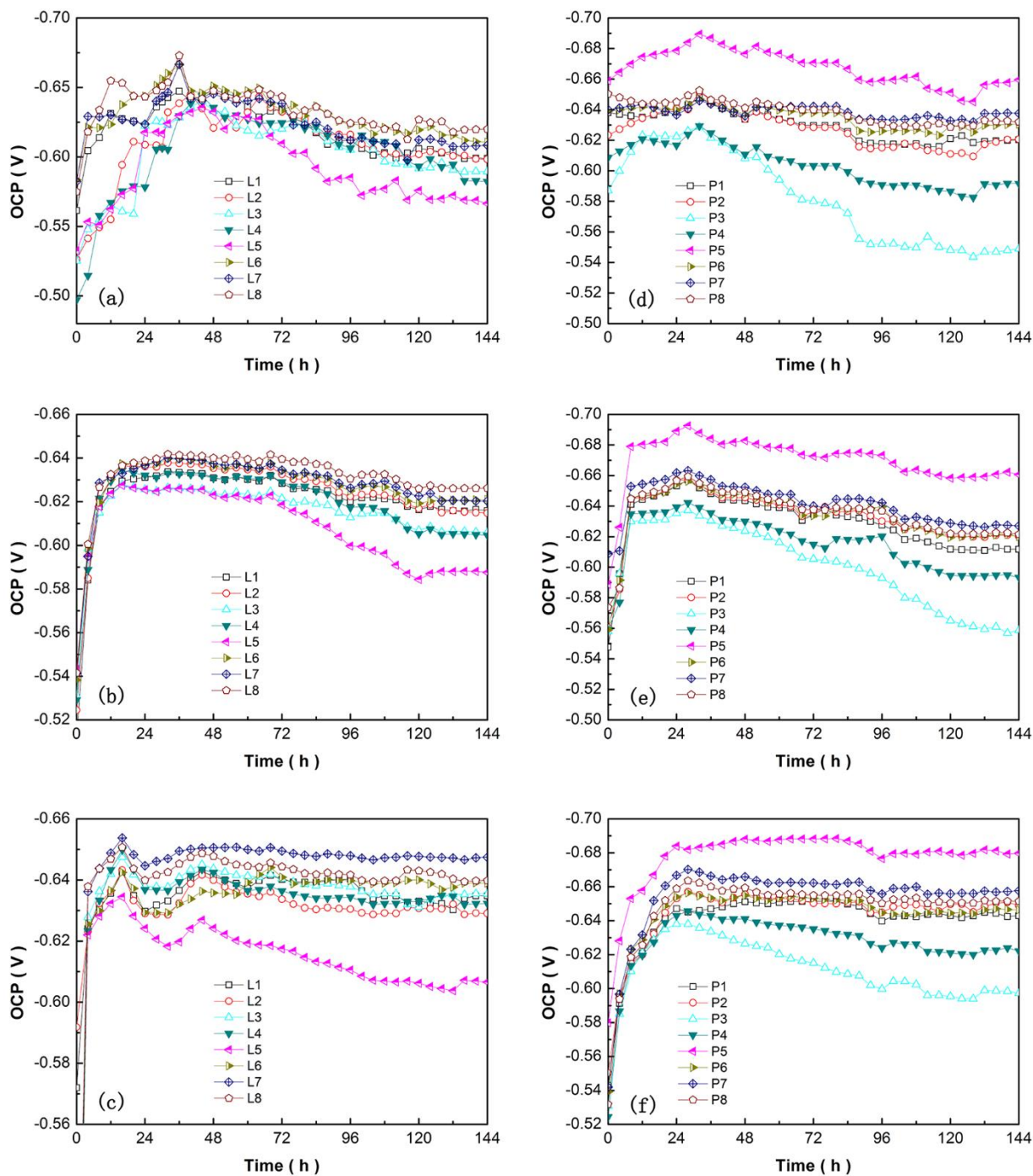


Figure 9. OCP measurements of L-type pipe fitting at inlet fluid flow velocities of 0.5 m/s (a), 1.0 m/s and (b), 1.5 m/s (c); and OCP measurements of P-type pipe fitting at inlet fluid flow velocities of 0.5 m/s (d), 1.0 m/s and (e), 1.5 m/s (f).

With the increase in the inlet velocity, the rules of corrosion become more apparent and more regular as presented in Fig. 9 (b, c, e, and f). Fig. 10 reveals the stable average OCP of each electrode after 144 h at three inlet velocities. It is apparent that the OCP decreases with the increase in inlet flow velocity; however, this can be explained by two factors. On the one hand, there is a larger flow rate

accompanied by greater wall shear stress, which scours surface coverings and makes it difficult to form a stable structure on the surface. On the other hand, compared with static immersion corrosion, it is found that the concentration of dissolved oxygen and other particles that participate in the electrode surface reactions in water under dynamic corrosion conditions is almost unchanged. This suggests that the concentration polarization effect is weakened[28], and the electrochemical corrosion cathodic reaction potential declines, whereas the metallic iron electrode potential remains, for the most part, unchanged. Accordingly, the overall result is that the OCP is reduced.

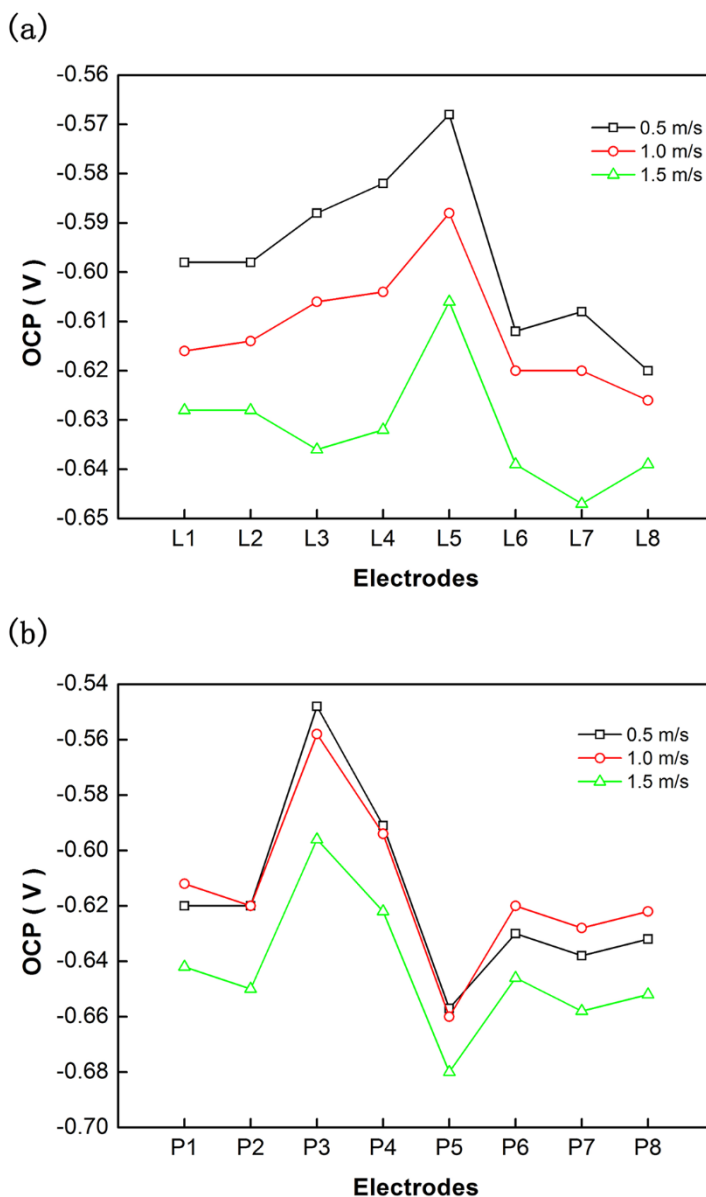


Figure 10. Stable average OCP of each electrode of L-type pipe fitting (a) and P-type pipe fitting (b) after 144 h at inlet fluid flow velocities of 0.5 m/s, 1.0 m/s and 1.5 m/s.

3.5 Corrosion Rate measurements

Similarly, to exclude the impact of the inherent differences of the electrodes, potentiodynamic

scanning was conducted under quiescent conditions. The corrosion rate results of the P-type pipe fittings are presented in Fig. 11, which indicates that during the initial 48 h, the corrosion rate changes dramatically with little regularity. What is unusual, however, is that the corrosion rate of the electrodes does not slow to a steady value later but rather fluctuates within a range of 0.08 to 0.12 mm/a, indicating that corrosion does not reach thermodynamic and kinetic stability simultaneously due to the random occurrence of non-uniform corrosion, as the surface condition of each electrode itself varies to some degree.

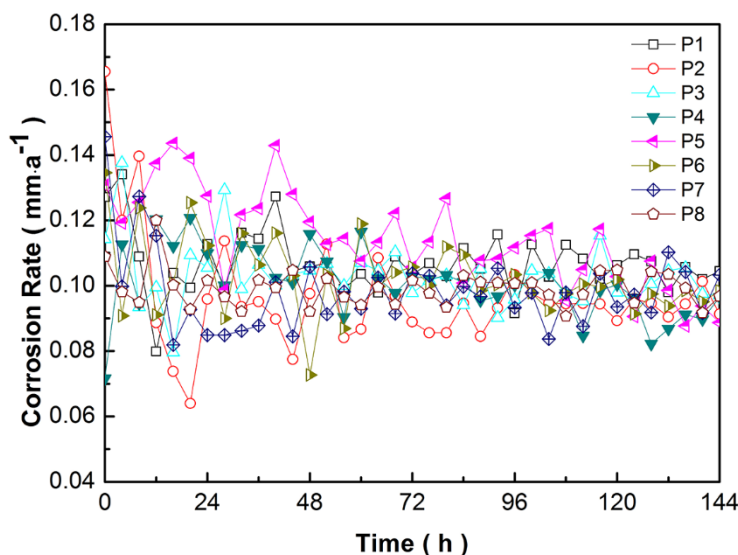


Figure 11. Corrosion rate of P-type pipe fitting in a stationary state.

Fig. 12 presents the corrosion rates of the L-type and P-type pipe fittings at three different inlet velocities. It is evident that the corrosion rates decrease over time. Although there are differences among every electrode, the difference is not substantial, and the corrosion rate distribution is relatively concentrated. Furthermore, pluralities of the study sites' corrosion rate curves decline in a linear manner. Therefore, it is hypothesized that electrode electrochemical reaction products and, less likely, intermediate products fail to promptly leave the electrode surface and that the accumulation of reaction products impedes the forward reaction rate or increase the reverse reaction rate. In addition to the accumulation of reaction products, another factor that must be considered is that the corrosion rate is calculated based on the density of the current corrosion measured by steady-state potentiodynamic scanning. Thus, the insulating barrier or the less conductive component that blocks the electron transfer may appear around the electrode surface[29]. As these two factors are independent of the electrode position and flow velocity, the decreases in corrosion rates are only possible with variances in the types of electrodes and in reaction times.

Fig. 13 presents the average corrosion rate of each electrode within a 144 h experimental period at three different inlet velocities. It is evident that the average corrosion rate increases as the fluid velocity increases and that increased velocity causes greater shear stress, which then weakens the accumulation effect of corrosion product coverings and inhibitory layers. Furthermore, water flow accelerates the mass transfer between the electrode surface and its surroundings[15, 30], i.e., primarily the diffusion of the

corrosion product and Fe^{2+} , which causes the continuous rapid diffusion of the intermediates and products of the iron, thus increasing the corrosion rate. It is further noted that the average corrosion rate under maximum velocity declines over time, suggesting that the cumulative effect of the reaction product continues to play a dominant role. It is also noted that for sites on the P-type pipe fitting, the distinction of the corrosion rate under the flow velocities of 0.5 m/s and 1.0 m/s is clear, which is inconsistent with the corresponding OCP distribution.

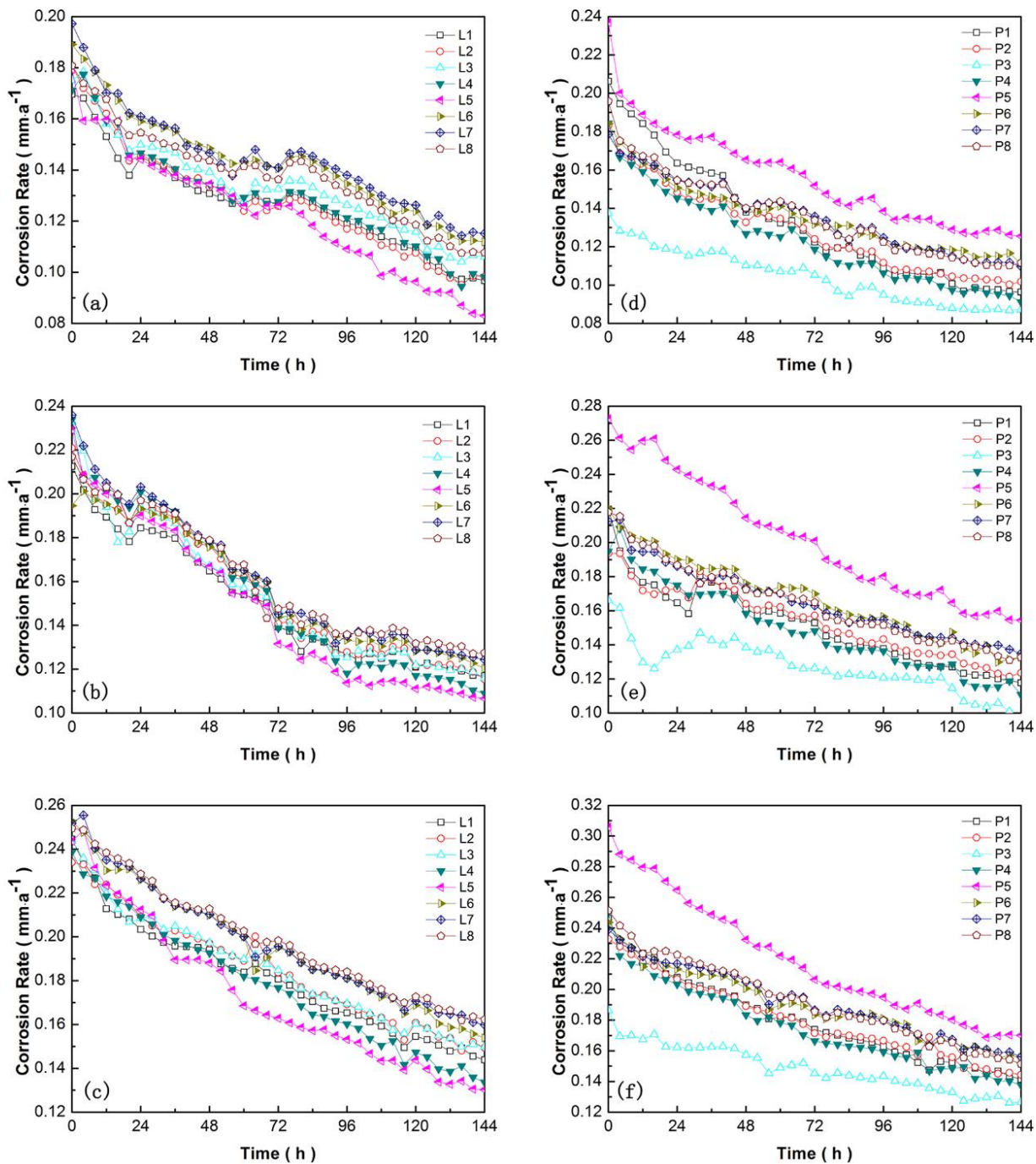


Figure 12. Corrosion rate of L-type pipe fitting at inlet fluid flow velocities of 0.5 m/s (a), 1.0 m/s (b), and 1.5 m/s (c), and corrosion rate of P-type pipe fitting at inlet fluid flow velocities of 0.5 m/s (d), 1.0 m/s (e), and 1.5 m/s (f).

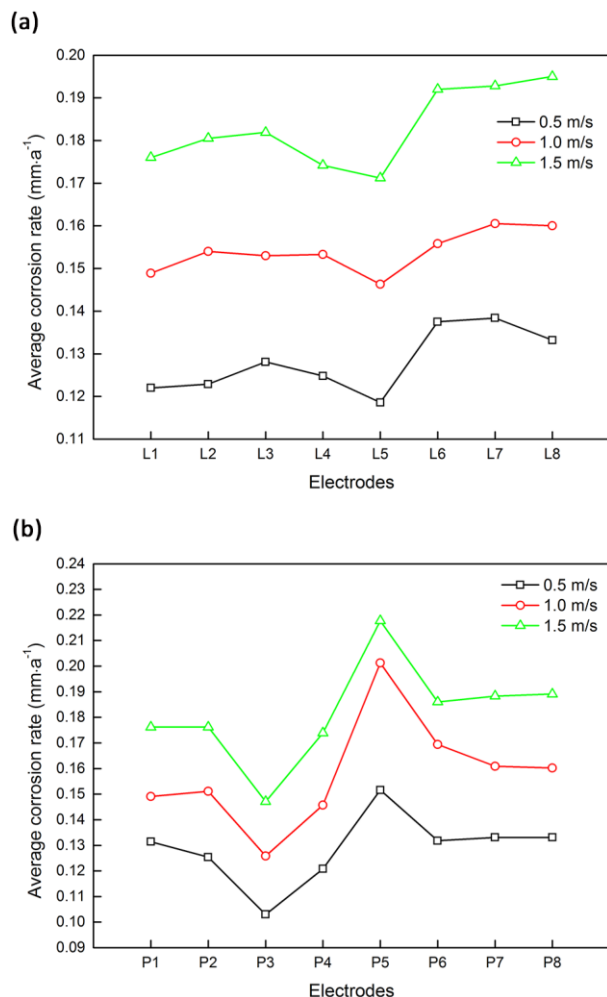


Figure 13. Stable average corrosion rate of each electrode of L-type pipe fitting (a) and P-type pipe fitting (b) after 144 h at an inlet fluid flow velocity of 0.5 m/s, 1.0 m/s and 1.5 m/s.

Thus, the OCP level cannot simply be used to determine the speed of the corrosion reaction. Whereas the effect of the flow rate on the OCP is not uniform, the effect on the corrosion rate is relatively uniform, which is the result of the combined effects of appropriate pressure and shear stress following flow rate changes.

The tendency of the corrosion rate to decline becomes more evident and more regular as the inlet velocity increases. Though the lowest corrosion rates are observed on electrodes L5 and P3, the corrosion rates of L4 and L5 are very close. Additionally, electrodes L6, L7 and L8 exhibit relatively large corrosion rates at approximately 0.110 mm/a when the inlet velocity is 0.5 m/s, whereas the corrosion rates of L1, L2 and L3 are approximately 0.105 mm/a. In the P-type pipe fitting, the corrosion rate of P5 is the highest, at approximately 0.125 mm/a. This is followed by the corrosion rates of P6, P7 and P8, all of which are approximately 0.110 mm/a, followed by P1, P2 and P4 whose corrosion rates are approximately 0.100 mm/a at an inlet velocity of 0.5 m/s (the above corrosion rates reflect the values at the end of the experiment). Fig. 14 shows the polarization curves of four typical electrodes (L5, L6, P3 and P5) after a 144-hour experimental period at three different inlet velocities.

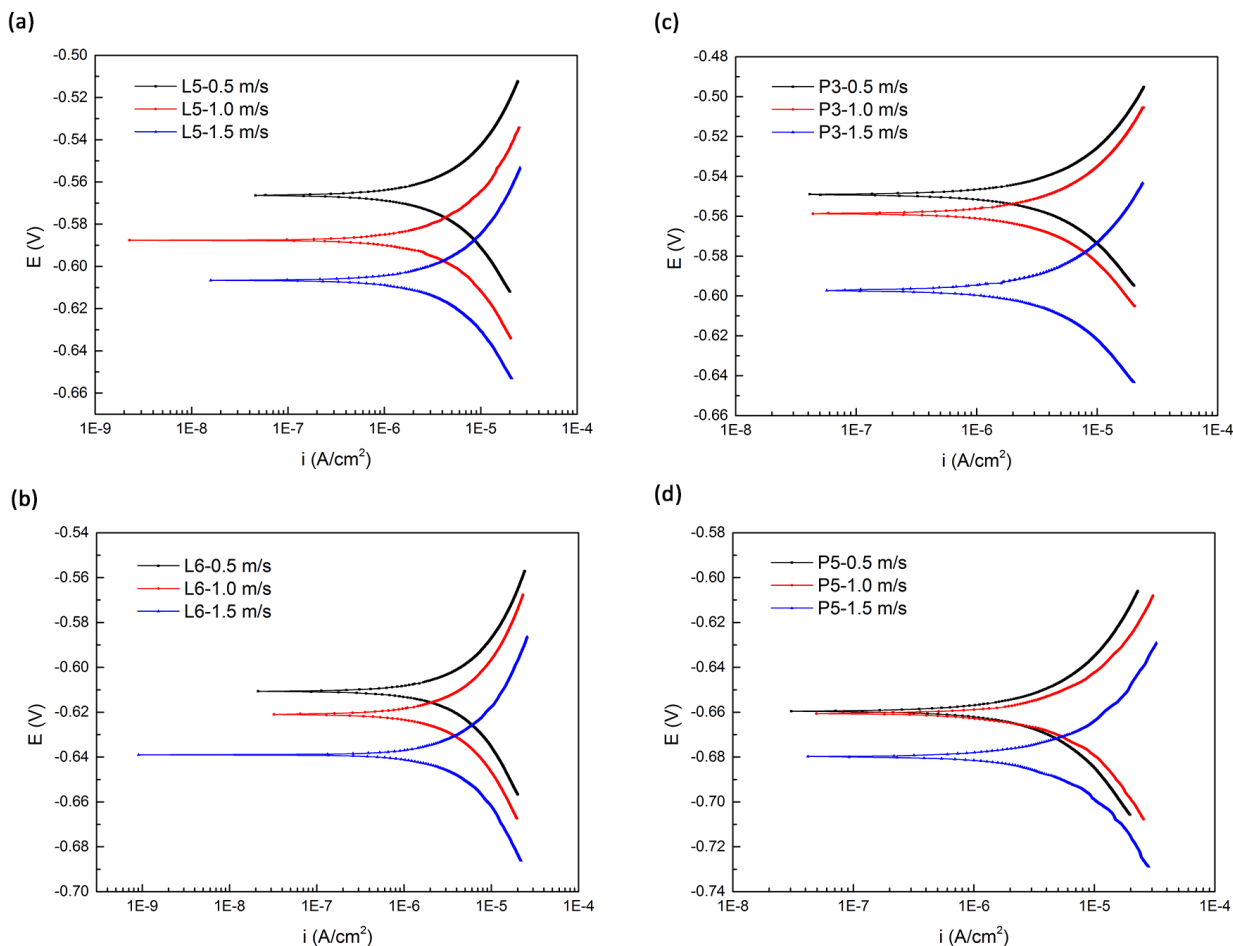


Figure 14. Polarization curves of L5 (a), L6 (b), P3 (c), and P5 (d) at an inlet fluid flow velocity of 0.5 m/s, 1.0 m/s, and 1.5 m/s.

Based on an examination of P5 and P3, it is determined that there exist tremendous differences in velocity, pressure and wall shear stress. For example, greater pressure, lower velocity and reduced wall shear stress lead to weaker corrosion, a finding that is consistent with previous research results[9]. Thus, it is concluded that corrosion rates at the top (or bottom) of the elbow and those on the outer side of the elbow are the lowest, followed by corrosion rates in the upstream straight section, whereas the corrosion rates on the downstream section are always higher than those in the upstream section. The highest corrosion rate occurs at the inner portion of the elbow due to the large flow velocity and the wall shear stress level[9].

3.6 Electrochemical impedance spectroscopy measurements

The EIS plots measured on the electrodes of the L-type and P-type pipe fittings under different inlet velocities are presented in Fig. 15.

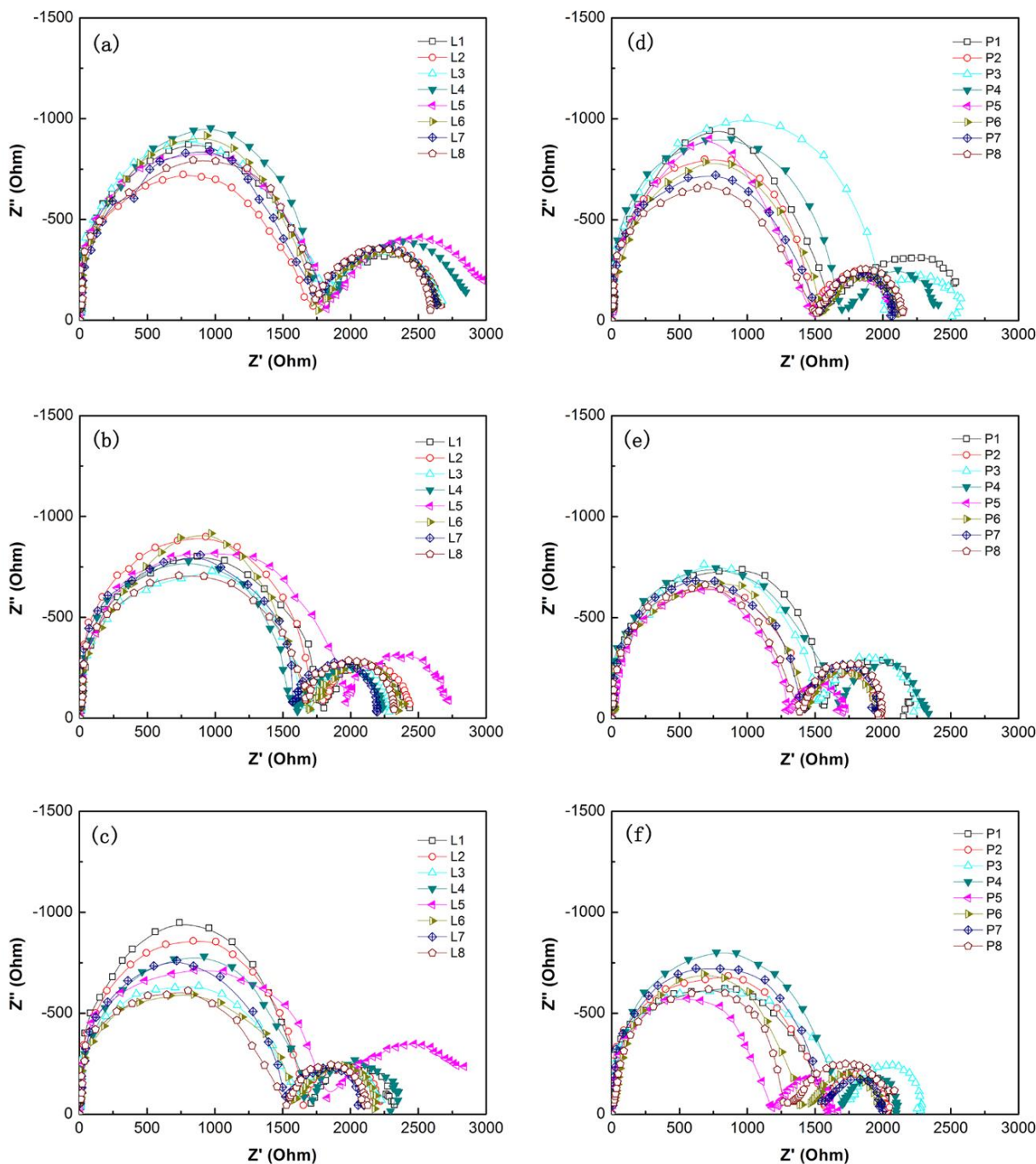


Figure 15. EIS plots measured on L-type pipe fittings at inlet fluid flow velocities of 0.5 m/s (a), 1.0 m/s (b), and 1.5 m/s (c), and EIS plots measured on P-type pipe fittings at inlet fluid flow velocities of 0.5 m/s (d), 1.0 m/s (e), and 1.5 m/s (f).

The point plot sequence is 100 kHz to 0.01 Hz from left to right. It is further noted that all plots exhibit an identical feature, i.e., one depressed capacitive semicircle in the high frequency range and another smaller one in the low-frequency range. Furthermore, when the inlet velocities increase, low-frequency capacitive arcs gradually shrink and the turning point of the high-frequency capacitive arc also move slightly inward, indicating the resistances decrease with the inlet velocities increase.

Fig. 15 (a, b, and c) indicate that among the capacitive arcs, the capacitive arc of L5 is located in

the outermost position, followed by, from outermost to innermost, L4, L1, L2, L3, L6 and L7, and L8. Similarly, as presented in Fig. 15 (d, e, and f), the capacitive arc of P3 is located in the outermost position, followed by, from outermost to innermost, P4, P1, P2, P6, P7 and P8, and P5. The results indicate preliminarily that the passive film on the ductile cast iron is strongest at the outermost portion of the elbow, followed by the upstream section, the downstream section and the innermost portion of the elbow. This phenomenon is consistent with the fluid flow regime in the pipe fitting. The CFD simulation results indicate that the water flow from the upstream straight pipe exhibits a steady and uniform flow to the elbow area, where a sudden change occurs in the flow direction that causes distribution differences in flow rate, pressure and wall shear stress. The water then flows to the downstream straight section where swirls and shunts appear.

According to the analysis and discussion of the OCP and corrosion rate, it is hypothesized that the film that covers the surface of the ductile cast iron electrode is generated during the dynamic electrochemical corrosion process. This speculation is demonstrated by the double capacitive arcs that occur in the impedance spectroscopy measurements. To analyse and obtain the resistance parameters, an electrochemical equivalent circuit presented in Fig. 16 is used to fit the EIS data where R_s denotes the solution resistance, Q_{dl} denotes the constant phase element (CPE) of the electrical double layer (EDL), R_{ct} denotes the charge transfer resistance of the EDL, Q_f denotes the CPE of the surface passivating film on the ductile cast iron, and R_f denotes the resistance of the surface passivating film of the ductile cast iron. Commonly, the variable in the high-frequency range of 100 Hz to 1000 Hz is ascribed to the protective passive film (corrosion products), which is in close contact with the surface of the metal working electrode, and the variable in the frequency range of 0.1 Hz to 10 Hz is associated with the electrical double layer between the metal working electrode and the corrosive media, i.e., tap water[23, 31].

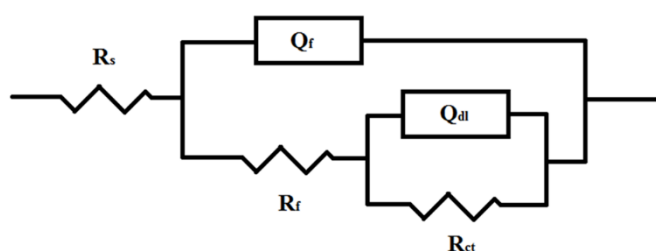


Figure 16. Equivalent circuit for EIS fitting.

The select fitted values R_{ct} and R_f are used to analyse corrosion variation, and the results are presented in Fig. 17. Fig. 17 indicates that the R_f value is higher than the R_{ct} value, suggesting that the corrosion product film on ductile cast iron surfaces is the primary controlling factor of the corrosion process when the flow velocity is below 1.5 m/s given dynamic corrosion. A reasonable explanation for this is that the formation of corrosion product film is affected greatly by the changes in the fluid field, as the wall shear stress differs at different locations of the pipe fitting under different flow velocities. However, the electric double layer structure and the electron transfer process were not significantly affected by the velocity.

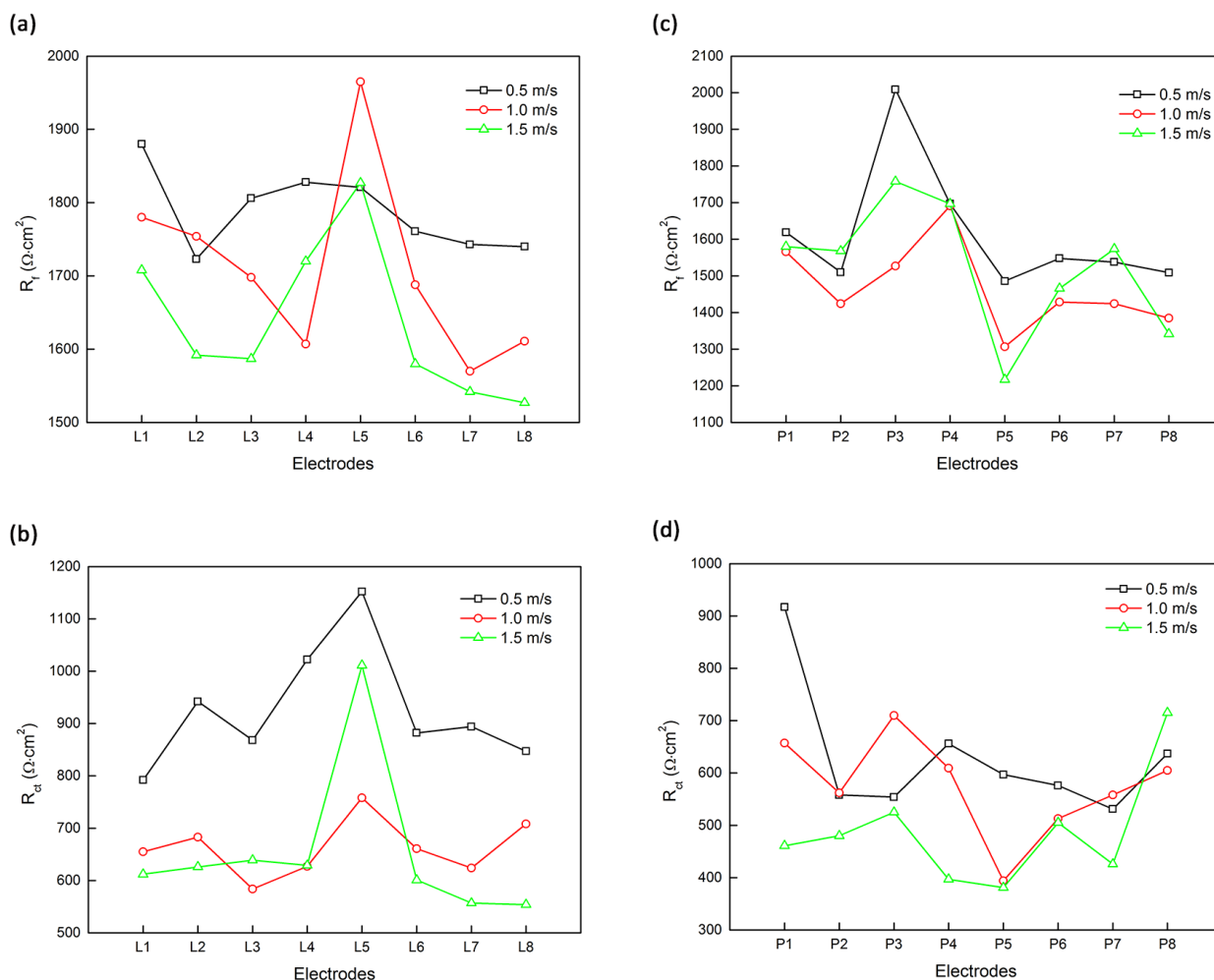


Figure 17. Fitted values of R_f and R_{ct} on L-type (a, b) and P-type (c, d) pipe fittings at an inlet fluid flow velocity of 0.5 m/s, 1.0 m/s, and 1.5 m/s.

In addition, it is noted that there are no clear rules on resistance values with variations in the flow rates. However, almost all points R_f values are substantially higher at a velocity of 0.5 m/s than they are at 1.0 m/s and 1.5 m/s, suggesting that a relatively thick compact film forms easily at 0.5 m/s. This may be due to the effect of wall shear stress, as low wall shear stress caused by low flow velocity is insufficient to scour off and destroy the corrosion product film. The variation patterns of the R_f values at 1.0 m/s and 1.5 m/s are likely attributable to the mixed influence of the location effect and the velocity effect as well as a more complete relationship between the flow velocity and the corrosion product film thickness; however, this requires further research. The charge transfer resistance, R_{ct} , undergoes changes that are roughly similar to those in R_f with the variation of flow velocity.

The impact rule, however, based on different point positions is upheld and almost unanimous under different flow rates. R_f and R_{ct} on electrode P5 are small, whereas on P3, P4 and L5, R_f and R_{ct} are relatively high, which suggests that it is not easy to form a thick and compact resistance film at the innermost side of the elbow, although at other locations, such as the outer side and the top (or bottom) of the elbow, the opposite is true. Furthermore, from the cross-sectional level, the R_f values at P1 and P2 are higher than the R_f values at P6, P7 and P8, indicating that the corrosion product film in the upstream

section is thicker and more compact than it is in the downstream section, and thus the corrosion is more severe in the downstream sections. However, the thickness of the corrosion product film at the top (or bottom) of the upstream and downstream sections does not differ significantly. These results are consistent with the discussion regarding the corrosion rate.

4. CONCLUSIONS

The dynamic corrosion of the ductile cast iron elbow in the water supply pipeline was investigated using a computational fluid dynamics (CFD) simulation and electrochemical measurements. The distribution of the flow velocity field, pressure field and wall shear stress of the pipe fitting are distinctly different among upstream straight sections, downstream straight sections and the elbow, regardless of whether it is at the inner or the outer portion and regardless of the different inlet flow velocity. It is demonstrated herein that there is a good correlation between the corrosion rate and the distribution of the hydrodynamics of the fluid flow at the elbow of the pipeline.

The use of corrosion product film on ductile cast iron surfaces is the main control factor inhibiting the corrosion process. The corrosion rate increases as the inlet fluid velocity increases, which causes higher wall shear stress to thin or degrade the corrosion scale. Moreover, when considering the position effect, corrosion behaviour occurs more easily at the innermost part of the elbow and the outer side of the downstream straight sections, and thus, the corrosion rate is higher due to high flow velocity, low pressure and substantial wall shear stress. The corrosion rate on the top (or bottom) and the outer side of the elbow, however, is relative low. Overall, the corrosion rate on the downstream section is higher than it is in the upstream section.

ACKNOWLEDGEMENTS

This work was supported by the National Natural Science Foundation of China (No. 51278333).

References

1. Y. Jiang, *Environ. Sci. Policy*, 54 (2015) 106.
2. C. Zheng, J. Gao, H. Tan, W. He and J. Zhang, Research on Urban Water Supply Pipeline Breakage Probability Model, International Conference on Pipelines and Trenchless Technology, Beijing, China, 2011, 927.
3. A. K. M. Hussain, A. A. Sanoussi, H. A. M. Hussain, C. A. Brebbia and A. M. Marinov, *Water Pollution X*, 135 (2010) 61.
4. J. Ahn, H. Lee, S. Kim, P. Kwak, J. Lee, H.S. Kim, J.F. Yang, T. Sekino, M. Anpo and S.W. Lee, Corrosion Control of Drinking Water Copper Pipes by Corrosion Inhibitor, 11th International Symposium on Eco-Materials Processing and Design, Osaka Prefecture Univ, Japan, 2010, 320.
5. A. Neville and C. Wang, *Wear*, 267 (2009) 2018.
6. K. C. Makris, S. S. Andra and G. Botsaris, *Crit. Rev. Environ. Sci. Technol*, 44 (2014) 1477.
7. Y. Yang, L. Wang and H. Wang, Design of Internal Corrosion and Residual Life of Water Supply Pipeline Simulated Experiment, 2012 International Conference on Electric Technology and Civil Engineering, Sanxia, China, 2012, 869.
8. G. A. Zhang and Y. F. Cheng, *Corros. Sci.*, 52 (2010) 2716.

9. G. A. Zhang, L. Zeng, H. L. Huang and X. P. Guo, *Corros. Sci*, 77 (2013) 334.
10. H. Hu and Y. F. Cheng, *J. Pet. Sci. Eng*, 146 (2016) 134.
11. S. Nešić and J. Postlethwaite, *Can. J. Chem. Eng*, 69 (1991) 698.
12. S. Nešić and J. Postlethwaite, *Can. J. Chem. Eng*, 69 (1991) 704.
13. H. P. Rani, T. Divya, R. R. Sahaya, V. Kain and D. K. Barua, *Ann. Nucl. Energy*, 69 (2014) 344.
14. Y. M. Ferng, *Nucl. Eng. Des*, 239 (2009) 231.
15. C.H. Lin and Y.M. Ferng, *Ann. Nucl. Energy*, 65 (2014) 214.
16. L.Y. Xu and Y. F. Cheng, *Corros. Sci*, 51 (2009) 2330.
17. M. El-Gammal, H. Mazhar, J. S. Cotton, C. Shefski, J. Pietralik and C. Y. Ching, *Nucl. Eng. Des*, 240 (2010) 1589.
18. K. Keshtkar, M. Nematollahi and A. Erfaninia, *Int. J. Hydrogen Energy*, 41 (2016) 7036.
19. L. Zeng, S. Shuang, X. P. Guo and G. A. Zhang, *Corros. Sci*, 111 (2016) 72.
20. Y. Zou, J. Wang and Y. Y. Zheng, *Corros. Sci*, 53 (2011) 208.
21. W. H. Ahmed, *Ann. Nucl. Energy*, 37 (2010) 598.
22. S. Nešić, *Corros. Sci*, 49 (2007) 4308.
23. J. Świetlik, U. Raczyk-Stanisławiak, P. Piszora and J. Nawrocki, *Water Res*, 46 (2012) 1.
24. J. F. Rios, J. A. Calderón and R.P. Nogueira, *Corrosion*, 69 (2013) 875.
25. E. Mohammadi Zahrani, A. M. Alfantazi, Corrosion behavior of alloy 625 in PbSO₄-Pb₃O₄-PbCl₂-ZnO-10 Wt pct CdO molten salt medium, Symposium on Fatigue and Corrosion Damage in Metallic Materials, San Diego, U.S.A, 2012, 2857.
26. A. G. Zelinsky, B. Y. Pirogov and O. A. Yurjev, *Corros. Sci*, 46 (2004) 1083.
27. T. L. Gerke, J. B. Maynard, M. R. Schock and D. L. Lytle, *Corros. Sci*, 50 (2008) 2030.
28. J. Liang, A. Deng, R. Xie, M. Gomez, J. Hu, J. Zhang, C. N. Ong and A. Adin, *Desalination*, 322 (2013) 76.
29. G. Palumbo, J. Banaś, A. Bałkowiec, J. Mizera and U. Lelek-Borkowska, *J. Solid State Electrochem*, 18 (2014) 2933.
30. Z. Liu, C. B. Liu, Y. G. Zheng, *Nucl. Power. Eng*, 30 (2009) 48.
31. S. J. Yuan, S. O. Pehkonen, Y. P. Ting, E. T. Kang and K. G. Neoh, *Ind. Eng. Chem. Res*, 47 (2008) 3008.